Earth and Planetary Science Letters 349–350 (2012) 186–197

Contents lists available at SciVerse ScienceDirect

Earth and Planetary Science Letters

journal homepage: www.elsevier.com/locate/epsl

Letters

Crustal structure and deformation of the SE Tibetan plateau revealed by receiver function data

Ya Sun [a,b,*], Fenglin Niu [b], Huafeng Liu [b], Youlin Chen [c], Jianxin Liu [a]

[a] School of Geosciences and Info-Physics, Central South University, Changsha, China
[b] Department of Earth Science, Rice University, Houston, TX, USA
[c] Array Information Technology, Greenbelt, MD, USA

ARTICLE INFO

Article history:
Received 28 February 2012
Received in revised form
3 July 2012
Accepted 5 July 2012
Editor: P. Shearer

Keywords:
SE Tibetan plateau
crustal anisotropy
lower crustal flow
depth varying deformation

ABSTRACT

We analyze a large amount of receiver function data recorded by regional seismic networks of the China Earthquake Administration to estimate crustal structure and deformation beneath the southeast margin of the Tibetan plateau and its surrounding areas. We develop a comprehensive analysis method that facilitates robust extraction of azimuthal seismic anisotropy from receiver function data. The method includes an estimate of fast polarization direction and splitting time by a joint analysis of radial and transverse receiver function data, and an evaluation of measurement reliability by statistical and harmonic analysis. We find significant seismic anisotropy with a splitting time of 0.5–0.9 s beneath the SE margin of the Tibetan plateau. Both the splitting time and fast polarization direction are comparable to those estimated from SKS/SKKS data, suggesting that crustal anisotropy is the main cause of shear wave splitting of the SKS/SKKS wave. This also suggests that deformation in the upper mantle is either weak or predominantly vertical, and is obviously different from the one in the crust. A vertical flow in the upper mantle, combined with the observation of a thin lithosphere beneath the study area, leads to the inference that part of the mantle lithosphere may have been removed and is descending into deep mantle. Stations located in the surrounding areas, on the other hand, exhibit very little to no crustal anisotropy. The estimated Moho depth and *Vp*/*Vs* ratio also show a distinct difference between the SE Tibetan plateau and the surrounding regions. Stations on the Tibetan plateau have a *Vp*/*Vs* ratio of ~1.79, which is substantially higher than those measured at the Yunnan–Guizhou (Yungui) plateau (~1.69). Our observations here are consistent with the scenario that the SE Tibet has been built by lower crustal flow. They also suggest that the mantle lithosphere beneath the margin may have been mechanically decoupled from the upper crust.

1. Introduction

The southeastern margin of the Tibetan plateau is located between the heartland of the plateau and the South China block, and spans most of Sichuan and Yunnan provinces and a part of Guizhou in southwest China (Fig. 1a). It is characterized by complex Cenozoic structures created during the India–Asia collision since ~50 Ma (Yin and Harrison, 2000). Two major models have been proposed to explain the deformation and uplift of this part of the plateau. In the first model, lateral extrusion of crustal blocks created the major strike slip faults in the region (e.g., Tapponnier et al., 1982), and in the second model lower crustal flow inflated the crust, causing the thickening of the crust and uplift of the plateau (e.g., Royden et al., 1997). From the block extrusion model, major deformation is expected to be localized along major shear zones. The latter model, on the other hand, predicts a diffuse deformation that can be observed widely across the margin. Both types of deformation have been observed with geological data, for example, Tapponnier et al. (1990) found that the Indochina block was displaced by at least 500 km southeastwards relative to the South China block along the Red River fault during the Oligo-Miocene. Incision data of the major rivers in the area, on the other hand, suggested an uplift occurring at regional scale after ~13 Ma (Clark et al., 2005). This broad deformtion was interpreted as evidence for lower crustal materials flowing from the center to the SE margin of the plateau (Schoenbohm et al., 2006).

Similarly, geophysical data are also elusive. Seismic tomography showed that the distribution of low velocity anomalies (LVAs) in the lower crust is very heterogenous (Wang et al., 2003). Although it seems that the observed LVAs somehow correlate

* Corresponding author at: School of Geosciences and Info-physics, Central South University, Changsha, Hunan, China. Now at Department of Earth Science, Rice University, Houston, TX, USA. Tel.: +1 713 348 2847; fax: +1 713 348 5214.
E-mail addresses: ys13@rice.edu, sunya0624@163.com (Y. Sun).

0012-821X/$ - see front matter © 2012 Elsevier B.V. All rights reserved.
http://dx.doi.org/10.1016/j.epsl.2012.07.007

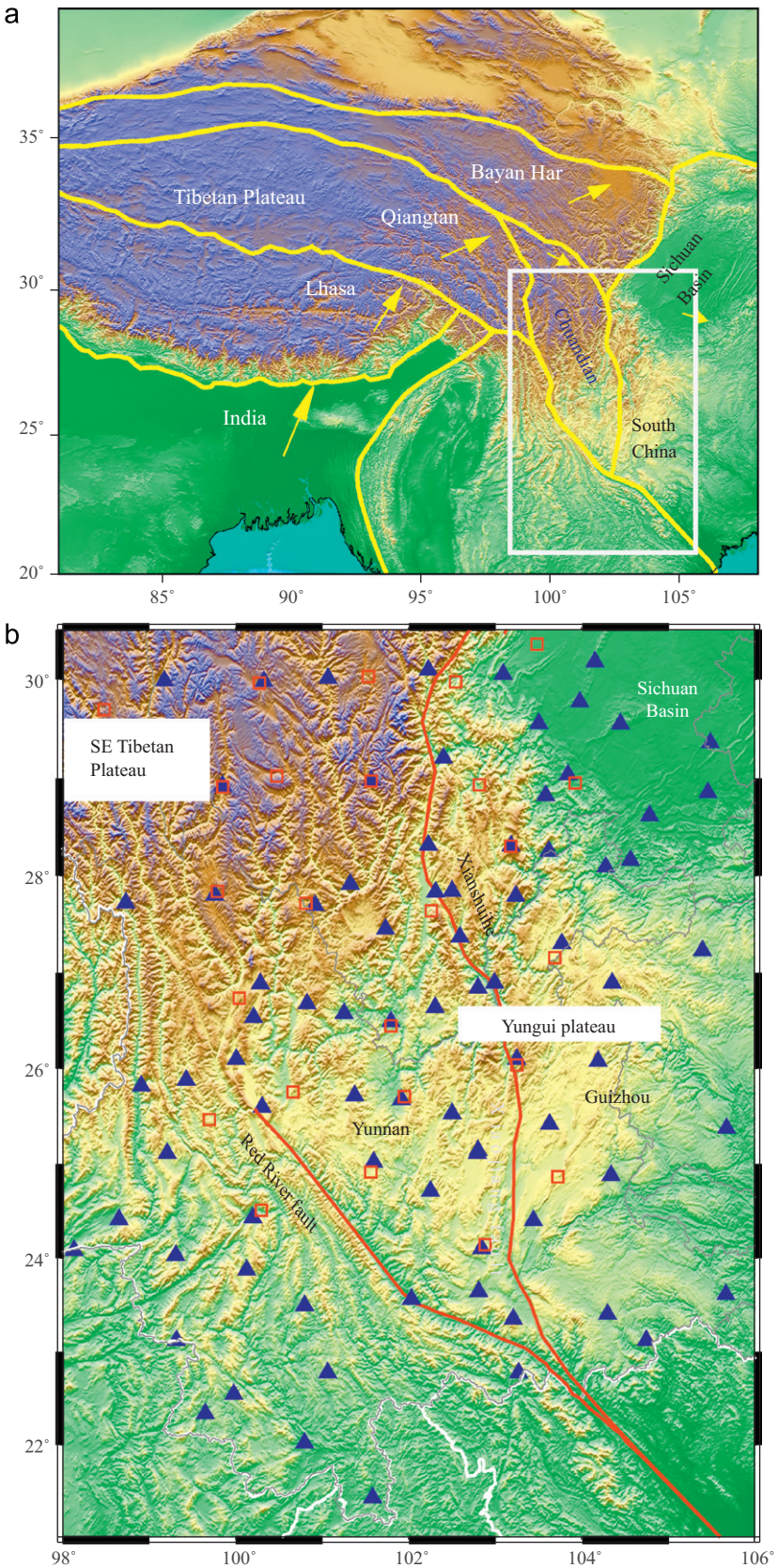

Fig. 1. (a) Map showing the surface motions of the India plate and different blocks within the Tibetan plateau relative to the stable Siberian craton. White box indicates the study region. (b) Topographic map showing the CEA broadband stations (solid blue triangle) and the PASSCAL stations (open red squares). Red lines indicate major faults in the area. (For interpretation of the references to color in this figure legend, the reader is referred to the web version of this article.)

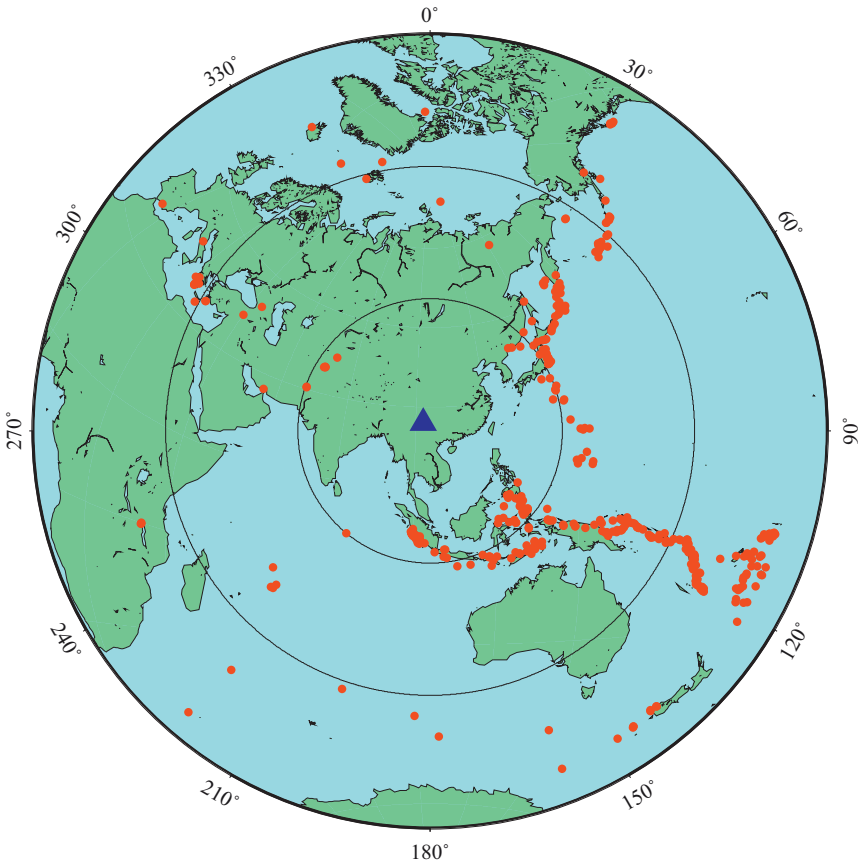

Fig. 2. Locations of the 413-teleseismic events (red solid circles) used in this study. Most of the earthquakes are located in the western and south Pacific, as well as the Indonesia subduction zones. Note that although some events fall into the 30° circle from the array center, all the seismograms we used have an epicentral distance between 30° and 90°. (For interpretation of the references to color in this figure legend, the reader is referred to the web version of this article.)

with the major fault systems in the area, the association between the LVAs and the proposed lower crustal flow is not so obvious. Magnetotelluric data, on the other hand, showed a wide distribution of channels with high electrical conductiviy at lower crustal depths across the margin (Bai et al., 2010). Thus the nature of deformation at depth beneath the region is still not well understood.

Questions also arise regarding the role that the lithospheric mantle plays during crustal thickening and surface uplift. Whether the mantle lithosphere deforms coherently with the crust or not is likely to have a very strong effect on crust dynamics. If surface uplift is caused mainly by inflation of the crust due to an active channel flow in the lower crust, then the mantle lithosphere and crust can deform differently as no substantial stress transfer can occur between them due to the low viscosity of the channel. On the other hand, if surface uplift and crustal thickening observed in the area are results of whole crustal shortening or block extrusion, then we will expect vertically coherent deformation across the entire lithosphere. Determining the depth distribution of deformation within the lithosphere thus becomes of great importance to understand the dominant orogenic process there.

Pervasive deformation can produce anisotropy on the scale of seismic wavelengths (e.g., Nicolas and Christensen, 1987; Mainprice and Nicolas, 1989). Measurements of seismic anisotropy thus can offer insight into the deformation kinematics within the Earth. Seismic anisotropy in Earth's upper crust is generally believed to be caused by stress-induced alignment of cracks. The cause of seismic aniostropy in the lower crust and mantle, on the other hand, is usually attributed to strain-induced lattice-preferred-orientation (LPO) of crustal and upper mantle minerals, such as mica, amphibole, and olivine. Because of its close relationship with the stress/strain field, seismic anisotropy has been widely used to quantify subsurface deformation associated with a wide range of tectonic processes (Crampin and Lovell, 1991; McNamara and Owens, 1993; Silver, 1996).

Both SKS waveform splitting and surface wave dispersion have been measured in the southeastern margin of the plateau to estimate seismic anisotropy (e.g., Lev et al., 2006; Wang et al., 2008; Yao et al., 2010). Lev et al. (2006) measured shear wave splitting of the core-refracted SKS/SKKS waves recorded by a temporary array of 25 stations in the area. Overall, the observed SKS/SKKS splitting times are of low amplitude, varying between 0.28 and 0.92 except for one station (1.2 s) with an average value of 0.58 s. The fast polarization direction exhibits a distinct transition from roughly the NS direction in the Tibetan plateau to mostly the EW direction in the Yunnan–Guizhou plateau (Yungui plateau). The deformation field in the mantle beneath the Yungui plateau apparently differs from the surface deformation field, suggesting a decoupled motion between the crust and mantle. On the other hand, the observed NS fast polarization direction agrees roughly with the surface deformation field, indicating that deformation within the lithosphere of the SE Tibetan plateau might be vertically coherent. Lev et al. (2006) argued that the source region of the observed seismic anisotropy from SKS/SKKS splitting data is likely located in the shallow mantle at ~60–160 km depth, which implies that seismic anisotropy in the crust is insignificant. Due to limited coverage in back azimuth, Lev et al. (2006) explained that multiple layers of anisotropy could not be ruled out with their dataset.

The P-to-S converted wave at the Moho, which can be extracted by receiver function analysis, is now widely used in measuring seismic anisotropy in the crust. In general, this conversion wave is registerd as a very weak signal in individual receiver functions. Making robust measurement of crust anisotropy with such a weak signal can be extremely difficult and dangerous. Recently, Liu and Niu (2012) developed a splitting measurement technique specifically for receiver function data. It utilizes the features that are uniquely possessed by anisotropic models observed on the synthetic receiver function data. We further added a harmonic analysis component to the method to enhance the evaluation of measurement reliability. We applied the technique to the broadband data recorded by regional seismic networks operated by the China Earthquake Administration (CEA). We selected a total of 79 stations located on the SE Tibetan plateau and its surrounding areas, including the Sichuan Basin, the Yunnan–Guizhou (Yungui) plateau and the fold belts further in the south. We measure crustal anisotropy, Moho depth and crustal *Vp*/*Vs* ratio at the 79 stations to constrain the average composition and deformation processes within the crust. The seismic measurements are then used to test the dynamic models mentioned above.

2. CEA regional network data

The data used in this study are collected from CEA's four provincial networks: Chongqing (CQ), Sichuan (SC), Yunnan (YN), and Guizhou (GZ). To study lateral variations in crustal structure and deformation of the SE Tibetan plateau and its surrounding areas, we choose 79 stations located in the region between 98° and 106° east, and 21° to 30.5° north (Fig. 1b). Several stations are very close to the sites of the IRIS-PASSCAL temporary array deployed by MIT and the Chengdu Institute of Geology and Mineral Resources (CIGMR) between 2003 and 2004. We select a total of 413 earthquakes within an epicentral distance of 30–90°, recorded between July of 2007 and July of 2010. These earthquakes provide very good coverage in both distance and azimuth (Fig. 2).

3. Methods

3.1. Receiver function generation and moveout corrections

To generate receiver functions, we first rotate the two horizontal components into radial (R) and transverse (T) components. Niu and Li (2011) found that a significant portion of the CEA regional network stations have orientation problems, so we use their method to compute the sensor orientation for each station before the rotation. We further rotate the radial (R) and vertical (Z) into the P and SV coordinates (e.g., Vinnik, 1977; Niu and Kawakatsu, 1998). We employ the "water-level" deconvolution technique to generate R, T, and SV receiver functions (e.g., Ammon, 1991; Pan and Niu, 2011). The R and T receiver functions are then used in harmonic analysis and the estimation of seismic anisotropy; while the SV receiver functions are used in the H–κ analysis. We visually inspect all the receiver functions and remove those with a low signal-to-noise ratio (SNR). At each station, we further calculate the covariance matrix of all the receiver functions and eliminate the ones that show a low cross correlation coefficient (<0.7) with other traces (Chen et al., 2010). The number of receiver functions selected at the 79 stations varies from 77 to 296, with an average of 220 (Table 1S).

The Moho Ps conversion phase has a slightly negative ray parameter relative to the direct P wave. The relative arrival time of the Ps thus has a negative distance moveout with respect to the direct P wave. We use the H–κ results to compute this moveout and make corrections so that all the Ps phases have a relative arrival time equivalent to the one with an epicentral distance of 60° and a source depth of 0 km. We further normalize the R and T receiver functions by dividing them by the peak amplitude of the P wave on the R component. After the moveout correction and the normalization, the R and T receiver functions are plotted as a function of back azimuth to detect systematic variations in the peak Ps arrival time and polarity changes in the R and T receiver functions.

3.2. Harmonic analysis of Ps arrival time

We first stack all the R receiver functions to get the average arrival time of the Moho Ps conversion phase, t_o. We then apply harmonic analysis to a time window with a length of t_L centered on t_o to find systematic variations in the arrival time of the Ps conversion as a function of back azimuth. Assuming a harmonic degree, n, with a peak-to-peak amplitude of δt, and initial phase of φ, the harmonic moveout correction at a station with a back azimuth of θ_i is

$$\delta t_i = \frac{\delta t}{2}\cos(n\theta_i+\varphi) \tag{1}$$

We then stack all the R receiver functions after correcting the harmonic moveout:

$$F_r(t,\varphi,\delta t) = \sum_{i=1}^{N} F_r^i(t-\delta t_i), \quad t\in[t_o-0.5t_L, t_o+0.5t_L] \tag{2}$$

The superscript i here represents the i-th receiver function, and N is the total number of receiver functions. We further compute the normalized maximum amplitude, maximum energy of the stacked receiver function, and minimum total residual between each receiver function and the stacked receiver function

$$A_{n,max} = \max\{F_r(t,\varphi,\delta t)\}/\max\{F_r(t,0,0)\}$$

$$E_{n,max} = \max\left\{\sum_{t=t_o-\frac{1}{2}t_L}^{t=t_o+\frac{1}{2}t_L} F_r^2(t,\varphi,\delta t)\right\}/\max\left\{\sum_{t=t_o-\frac{1}{2}t_L}^{t=t_o+\frac{1}{2}t_L} F_r^2(t,0,0)\right\}$$

$$R_{n,min} = \min\left\{\frac{1}{N}\sum_{i=1}^{N}\sum_{t=t_o-\frac{1}{2}t_L}^{t=t_o+\frac{1}{2}t_L}\left[F_r(t,\varphi,\delta t)-F_r^i(t,\varphi,\delta t)\right]^2\right\}/\min \times\left\{\frac{1}{N}\sum_{i=1}^{N}\sum_{t=t_o-\frac{1}{2}t_L}^{t=t_o+\frac{1}{2}t_L}\left[F_r(t,0,0)-F_r^i(t,0,0)\right]^2\right\} \tag{3}$$

here $A_{n,max}$ and $E_{n,max}$ represent the maxima of the normalized peak amplitude and total energy of the stacked receiver function. $R_{n,min}$ is the minimum of the summed residual between the stacked receiver function and the individual receiver functions. $A_{n,max}$, $E_{n,max}$, and $R_{n,min}$ are taken from the entire Ps conversion time window, and the entire (φ, δt) domain. We varied n from 1 to 8, φ in the range of 0–360° with an increment of 1°, and δt from 0.0 to 1.5 s with increments of 0.02 s.

An example of the harmonic analysis is shown in Fig. 3b. The maximum amplitude and energy of the stacked receiver function, as well as the best fit between the stacked and individual receiver functions have a distinct peak at degree-2. As many studies (e.g., Levin and Park, 1997; Peng and Humphreys, 1997; Savage, 1998; Shiomi and Park, 2008) have shown, several types of crustal structure, such as a dipping Moho, P-wave anisotropy or azimuthal S-wave anisotropy with an inclined axis, can result in a degree-1 back azimuthal variation. On the other hand, azimuthal S-wave anisotropy with a horizontal axis can register a Ps signal

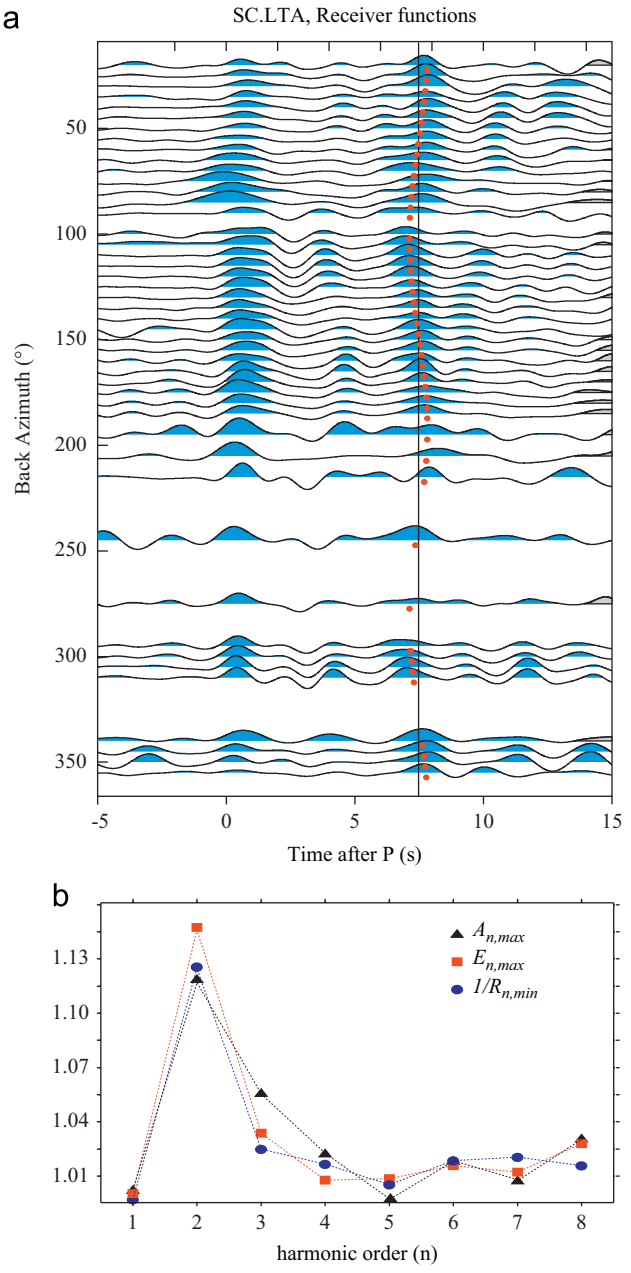

Fig. 3. (a) SV receiver functions recorded at station SC.LTA are plotted as a function of back azimuth. The receiver functions here are stacked in 10° bins along the back azimuth direction. Solid line indicates the average arrival times of the primary P to S conversion phase, and red dots represent the azimuthal variation in its arrival time. (b) Results of the harmonic analysis at the same station. The maximum value of peak amplitude and total energy, as well as the reciprocal of the minimum residual are shown as a function of the harmonic degree. Note the peak at the degree-2, indicative of azimuthal seismic anisotropy with a horizontal axis in the data. (For interpretation of the references to color in this figure legend, the reader is referred to the web version of this article.)

that has a degree-2 back azimuthal variation in arrival time. Small-scale azimuthal variations in crustal velocity and Moho topography may result in higher order harmonic variations.

3.3. Estimate of crustal anisotropy

When radially polarized S waves propagate through an anisotropic crust with a horizontally symmetrical axis, their energy is split and part of it is projected onto the transverse component. The birefringent T waveforms are proportional to the time derivative of those on the R component. In addition, the arrival time and the polarity of the S wave on both the R and T components each exhibit a four-lobe (degree-2) variation pattern along the back azimuth direction. These two unique features of azimuthal anisotropy provide a strong base for resolving it from other heterogeneous structures, such as velocity heterogeneities in the crust and a tilted crust–mantle boundary.

Although we make anisotropy measurements at all the stations, we only select the results of the stations that exhibit a strong degree-2 azimuthal variation. The method used here was developed by Liu and Niu (2012). Here we briefly review the major steps they proposed to better constrain azimuthal anisotropy with receiver function data. The method includes computing three individual and one joint objective functions, and a statistical analysis of the reliability of the estimated anisotropy. The individual objective functions (IOFs) are designed to search for a pair of φ and δt that (1) maximize the peak energy of the stacked R receiver function after a cosine moveout correction in the Ps arrival time; or (2) maximize the cross-correlation of the radial receiver functions after a full correction of crustal anisotropy; or (3) minimize the total energy of transverse receiver functions stacked after a removal of crustal anisotropy. The joint objective function (JOF) is computed by taking the average of the three IOFs, while the statistical analysis utilizes the principle that stacking a total of N coherent signals can lead to an increase of SNR by a factor of $N^{1/2}$. Further information on the method can be found in Liu and Niu (2012).

In Fig. 4, we show the results measured at station SC.LTA. The three IOFs are shown in Fig. 4a–c. The fast polarization direction and the splitting time estimated from the three methods are in good agreement with each other. The JOF estimate is closer to the value estimated from the transverse component because of the large maximum value of the third IOF. As discussed in Liu and Niu (2012), the maxima (the difference between maxima and unit value) of the three IOFs and the subsequent JOF are proportional to splitting time. The large maximum amplitude of the JOF obtained here is thus a strong manifestation of crustal anisotropy beneath the station. Results of the statistical analysis of the measurement reliability based on the T and R receiver functions are shown in Fig. 4e and f, respectively. The analysis with the T receiver functions indicates that the SNR of the data stacked after a correction of waveform polarity roughly increases linearly with $N^{1/2}$ (open squares in Fig. 4e) while the SNR of those stacked without a correction of waveform polarity remains nearly flat across the whole range of $N^{1/2}$ (open circles in Fig. 4e). On the other hand, once anisotropy is removed, the T receiver functions are composed primarily of random noise, leading to a flat distribution of SNR no matter whether a polarity correction (filled squares in Fig. 4e) is applied or not (filled circles in Fig. 4e). If anisotropy is signficant, then the stacked R receiver functions after the correction of crustal anisotropy (filled triangles in Fig. 4f) are expected to have a larger *SNR* than those without correction (open triangles in Fig. 4f).

In Fig. 5, we show part of the SV and T receiver functions before and after the correction of the estimated crustal anisotropy. From the original SV receiver function, we can see a clear azimuthal variation in the Ps arrival time (Fig. 5a). The Ps conversion phase can also be seen on the T receiver functions, with a clear change in waveform polarity (Fig. 5b). These features are no longer seen from the data once seismic anisotropy is corrected. More specifically, the Ps converted phase arrives roughly at the same time on the radial component, and there are no obvious Ps arrivals on the transverse component (Fig. 5c and d).

3.4. Depth stacking and H–κ analysis

We also apply H–κ stacking to all the stations to determine the Moho depth and the average Vp/Vs ratio (κ) of the crust. To do so,

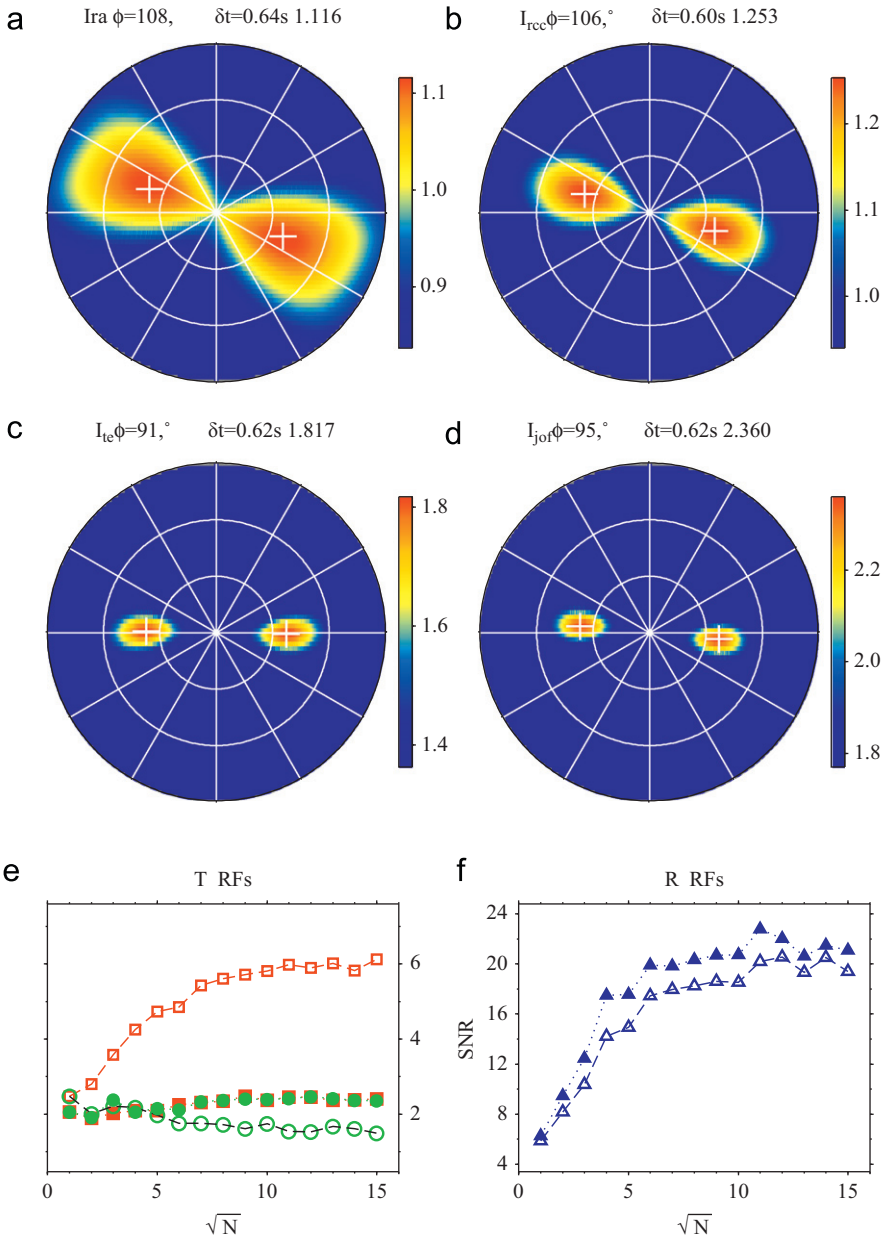

Fig. 4. Results from the joint analysis of crustal anisotropy at station SC.LTA. (a), (b), and (c) correspond to three different methods for estimating seismic anisotropy: (1) R energy maximization with a cosine moveout correction; (2) radial cc maximization; and (c) T energy minimization (represented by maximizing the inverse of T energy). Color scales showing variations of the objective functions are plotted to the right of the functions. The JOF is shown in (d). The objective functions were computed in a 2D plane of (φ, δt) in the range of (0–360°, 0.0–1.5 s) with an increment of (1°, 0.02 s). (e) and (f) show the reliability analysis of the estimated anisotropy with the T and R receiver function data, respectively. Open and filled symbols in (e) and (f) represent SNR calculated from stacks of receiver functions before and after the removal of seismic anisotropy determined by the JOF. Note the steady increase of square (stack with a sign correction of back azimuth) with increasing $N^{1/2}$ in (e) and that the filled triangles are always above the open ones in (f). (For interpretation of the references to color in this figure, the reader is referred to the web version of this article.)

we employ the method proposed by Niu et al. (2007). We first use a depth stacking method to determine an initial depth for the Moho beneath a station. We then employ a refined H–κ analysis to determine the final estimates of depth and Vp/Vs that best match the observed P to S conversion and the reverberation phases. To obtain the initial depth, we first gather receiver functions recorded at each station and make a time to depth conversion by assuming that P to S conversions are the primary sources of energy in the P-wave coda window. For a conversion depth, d, we first compute the relative arrival time of the converted phase, *Pds*, with respect to the direct arrival by ray tracing the two phases using a modified 1D iasp91 velocity model (Kennett and Engdahl, 1991), which has a crust extending to depth d. We then sum the receiver function values averaged in a 0.1 s window centered on the arrival time of *Pds* using both linear and non-linear stacking technique (e.g., Muirhead, 1968; Kawakatsu and Niu, 1994). We vary d from 0 to 100 km with an increment of 1 km and use the depth with maximum amplitude as the initial Moho depth. The stacked depth profile at station SC.LTA is shown in Fig. 6a. We can see a clear P-to-S conversion peak at depth around 61 km.

The estimated crustal thickness, H, by the above depth stacking method, depends on the reference velocity model. There is a complete trade off between H and the Vp/Vs ratio, and Vp (Nair et al., 2006). Adding the two crustal multiples (2p1s and 1p2s, Niu and James, 2002) in the stacking can, in principle, resolve the trade off (Zhu and Kanamori, 2000). In most of the studies, however, the two multiples are assigned a low weight in the

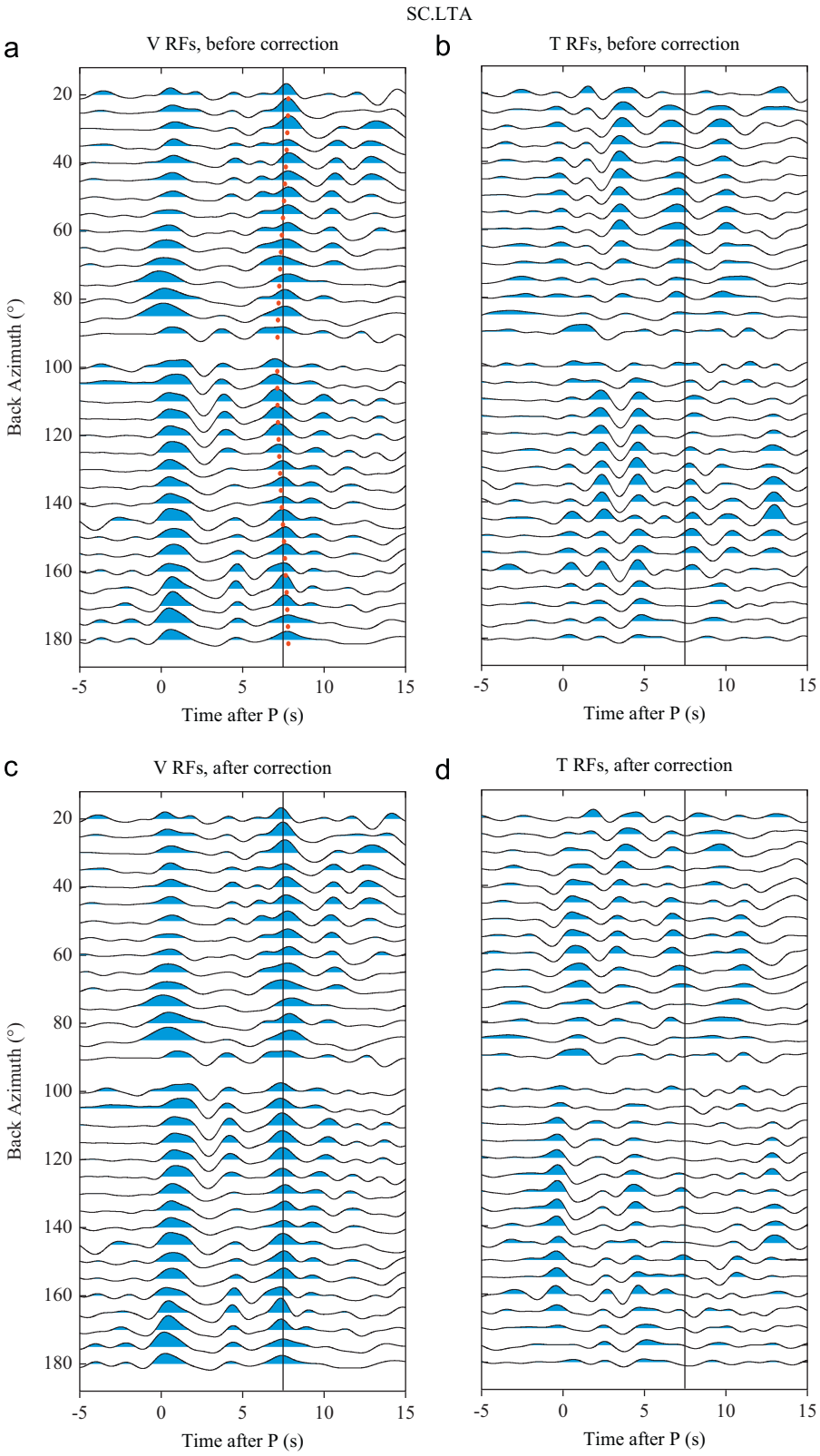

Fig. 5. A comparison between receiver functions before (a, b) and after the correction (c, d) of seismic anisotropy. Receiver functions shown here are recorded at station SC.LTA and are binned in 10° azimuthal caps. The solid line indicates the average arrival time of the Moho Ps converted phase. The SV and T components before correction of anisotropy are shown in (a) and (b), respectively. Dots in (a) indicate the arrival time of the peak amplitude of the Moho Ps converted phase. Note its cosine variation along the back azimuthal direction in (a), and the polarity changes of the Ps phase in (b). The SV and T receiver functions after the removal of anisotropy are shown in (c) and (d), respectively. Note the good alignment of the Ps after the correction in (c), and the low energy along the line of the Ps arrival time window in (d) after the contribution of seismic anisotropy has been removed.

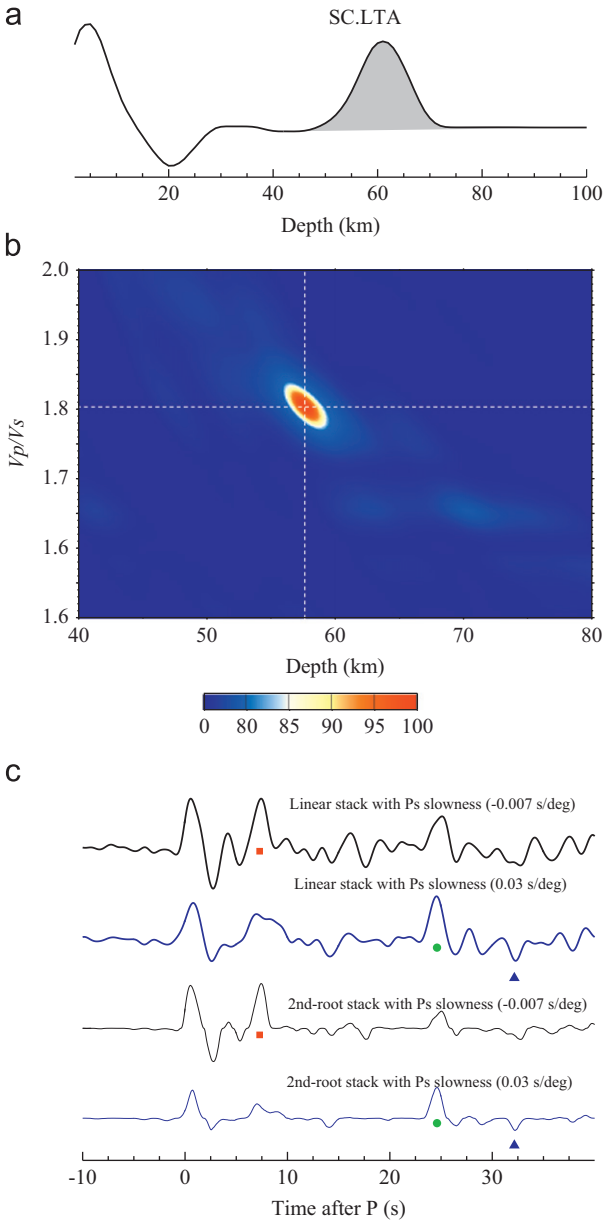

Fig. 6. (a) The stacked receiver function after the time-to-depth conversion at station SC.LTA. The peak of the Ps conversion is at 61 km. (b) Results of the H–κ analysis obtained from SC.LTA. Color contours show the summed amplitude as a function of crustal thickness and Vp/Vs ratio. The two white lines indicate location of the amplitude peak. (c) Stacked receiver functions with the Ps slowness (the first and third traces) and the 2p1s slowness (the second and fourth traces). The top two traces are obtained by a linear stack while the bottom two are computed from a 2nd-root stack. The square, circle, and triangle indicate the Ps, 2p1s and 1p2s phase, respectively. Note that amplitude of the phases is larger when they are stacked with the correct slowness. (For interpretation of the references to color in this figure, the reader is referred to the web version of this article.)

stacking due to the low SNR of the two phases. This can introduce large trade off between H and κ. Niu et al. (2007) introduced a coherence index of the three phases, $c(\kappa)$, to reduce the H–κ tradeoff

$$s(H,\kappa)=\frac{c(\kappa)}{N}\sum_{i=1}^{N}\{w_1 r_i(t_1)+w_2 r_i(t_2)-w_3 r_i(t_3)\} \quad (4)$$

here N is the number of receiver functions at a given station and $r_i(t)$ represents the amplitude of the ith receiver function at the predicted arrival times of the primary P-to-S converted phase *0p1s* (*t1*), and the two crustal multiples, *2p1s* (*t2*) and *1p2s* (*t3*). w_1, w_2, and w_3 are the weights of the three phases and are assigned 0.5, 0.25, and 0.25, respectively. We search for H within $\pm$20 km of the initial depth determined from the depth stacking. κ is varied in the range of 1.5–2 with an increment of 0.001. H and κ ratio are finally determined by picking the location where the summed amplitude, $s(H,\kappa)$, reaches its maximum. For each station, we use a 1D P-wave velocity model derived from a 3D traveltime tomography study (Sun and Toksoz, 2006).

The H–κ stacking result at SC.LTA is shown in Fig. 6b, which shows a well-defined peak at (H=57.8 km, κ=1.803). We further compute the vespagram of the SV receiver functions to measure the slowness of the Ps and the multiples. To do so, we stacked the receiver functions with linear moveout corrections corresponding to a range of slownesses (e.g., Kawakatsu and Niu, 1994). The measured slowness of the Ps and multiples are negative and positive (Fig. 6c), respectively, which is expected due to the slight differences in ray paths with respect to the direct P wave.

4. Results and discussion

We obtained 78 measurements of crustal thickness (H) and 74 measurements of Vp/Vs ratio (κ) from the 79 stations. The results are listed in Table 1S. The table is organized by grouping stations in the following tectonic/physiographic regions (Fig. 7): the Sichuan Basin (SB), the Tibetan plateau (TP); the Yungui plateau (YG); the Western Yunnan Fold Belts (WB), which include the Tengchong block, Changning–Menglian Belt, Lanping–Simao Fold System, Ailaoshan Belt; and the South China Fold System (SF). We further computed Moho depth from the sea level (D) by subtracting station elevations from the measured H. The measured Moho depth and Vp/Vs ratio are further interpolated into meshed $0.2^\circ \times 0.2^\circ$ grids of the study area between 21.0°N to 30.4°N in latitude and 98.0°E to 106.0°E in longitude. The interpolation is performed to fit a flattest Moho with an inversion method (Niu et al., 2007). There are 41 and 48 grid points in the longitudinal and latitudinal directions, respectively, within the study area. This gives a total of 1968 unknown parameters of D and κ, which are inverted from the 78 and 74 observations, respectively. A regularization that minimizes the first derivative of the model is added to regularize the underdetermined inversion. The results are shown in Fig. 7. Since there are essentially no stations in the southeast and southwest corner of the study area, the maps may not reflect the true values of the Moho depth and Vp/Vs ratio for these two corners.

We also include measurements from 9 PASSCAL stations in the interpolation. 8 stations (MC04, MC07, MC13, MC10, MC12, MC18, MC21 and MC25) were installed by MIT/CIGMR and another 1 station (ES28) was deployed by Lehigh University in 2003 and 2004. Xu et al. (2007) analyzed the receiver function data recorded by the MIT/CIGMR array and estimated crustal thickness and average crustal Vp/Vs beneath 22 stations. In general, our measurements are in good agreement with their results. The measured crustal thickness here is also consistent with the results of surface wave studies by Yao et al. (2008, 2010).

4.1. Moho depth

We have a total of 13 stations (including 3 PASSCAL stations) located on the core part of the Tibetan plateau with an elevation above 2500 m in western Sichuan province. The estimated Moho depth varies from 48.8 km to 71.1 km, with an average depth of 61 km, which is significantly higher than the surrounding regions. The thinnest crust in the study area is found at the southwestern border on the Changning–Menglian Belt, which is about 32 km.

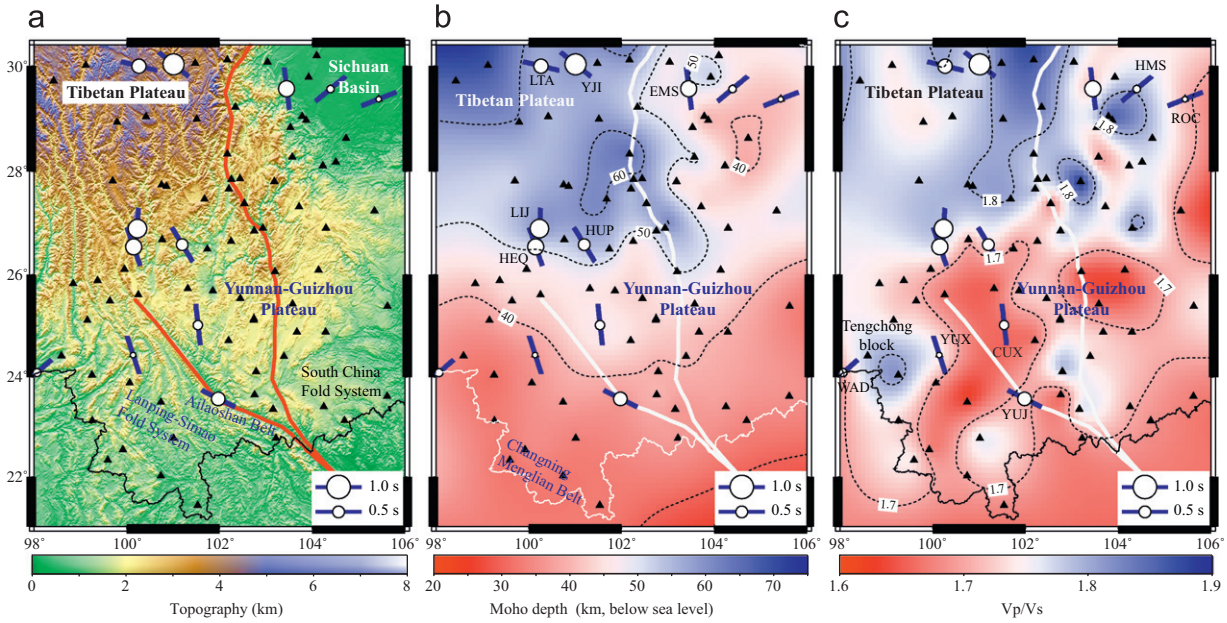

Fig. 7. Maps showing the surface topography (a), Moho topography (b), and the lateral variations of the *Vp*/*Vs* ratio (c). The color contour is calculated from observations at stations shown by black triangles. Note the large contrast in Moho depth and *Vp*/*Vs* ratio between the Tibetan plateau and the rest of the study area. In particular, the Tibetan plateau shows a higher *Vp*/*Vs* (~1.79) ratio than the Yungui plateau (~1.69), suggesting that it has relatively more mafic lower crustal materials. Also shown on the map are the 12 measurements of the fast directions and splitting times. The fast-axis direction is shown by a bar line, and the amount of splitting is indicated by the size of the circle plotted at the location of each station. Note the large splitting times from the 6 stations located at the SE Tibetan plateau. Station YUJ (YN.YUJ) located near the Red River fault also shows a large splitting time (0.58 s).

A moderately thick crust also underlies stations located on the South China Fold System with a Moho depth in the range of 35.1–38.3 km (Table 1S, Fig. 7). Moving toward the north, in the Yunnan–Guizhou plateau, which has an elevation of ~1.7 km, the crust thickens from ~41 km in the south to ~50 km at its northern border (Table 1S, Fig. 7). The thinnest crust within the Sichuan Basin is found at its southern end, with a thickness of approximately 40 km. The Moho beneath the basin deepens gradually towards northwest, and reaches to more than 50 km at its northwestern edge (Table 1S, Fig. 7). All of the receiver functions show significant P to S conversion and multiple reflections between the free surface and the sedimentary–bedrock boundary located at a few to ten kilometers beneath the surface. Watson et al. (1987) suggested that the Sichuan plateau is a flexural basin controlled by southeastward thrusting along its northwestern margin. The observed thickening of the sedimentary cover and crustal thickness towards the northwest agrees with their interpretation of the origin of the Sichuan basin. Overall we observe a gradual thickening of the continental crust from southeast to northwest (Fig. 7b).

4.2. *Vp*/*Vs* ratio

The measured *Vp*/*Vs* ratio also shows significant differences between the Tibetan plateau and its surrounding areas, especially the Yungui plateau. The average *Vp*/*Vs* ratio calculated from the 13 stations with high elevation (> 2500 m) is 1.79, while *Vp*/*Vs* ratio averaged over the stations located on the Yungui plateau is only 1.69 (Table 1S, Fig. 7c). We observe a wide range of *Vp*/*Vs* ratios across the Sichuan basin (Table 1S, Fig. 7c). We attribute such a variation to the changes in sediment thickness within the basin. In general, sediment has a very high *Vp*/*Vs*, and the measured *Vp*/*Vs* ratio is a weighted average between sediment and the igneous bedrocks in a crustal column. When the proportion of sediment in the column is high, then the estimated *Vp*/*Vs* ratio is expected to be high. For example, the western part of the basin has a thick sediment cover; the observed *Vp*/*Vs* ratio there is much higher than that of the eastern side of the basin. According to Pan and Niu (2011), the NE margin of the Tibetan plateau, north to the study area here, also shows a very low crustal *Vp*/*Vs* ratio, ~1.69, nearly similar to the one observed beneath the Yungui plateau. Therefore, comparing to the surrounding area, the SE Tibetan crust has a distinct *Vp*/*Vs* ratio. We further argue this difference is likely caused by composition.

The ratio of compressional to shear wave velocities has been found by laboratory studies to be useful in constraining the composition of material sampled by seismic waves as varying compositions can have similar *Vp* or *Vs* values but different *Vp*/*Vs* (e.g., Christensen, 1996). The relative abundance of quartz (*Vp*/*Vs* = 1.49) and plagioclase (*Vp*/*Vs* = 1.87) has a dominant effect on the *Vp*/*Vs* ratio of common igneous rocks and their metamorphosed equivalents. An increase in plagioclase content or a decrease in quartz content can increase the *Vp*/*Vs* ratio of a rock. For example, the *Vp*/*Vs* ratio increases from 1.710 for granitic rock, to 1.78 for diorite, and to 1.87 for gabbro (Tarkov and Vavakin, 1982). Mafic/ultramafic igneous rocks generally have high *Vp*/*Vs* ratios because they usually contain gabbro and peridotite or dunite. On the other hand, felsic rocks possess a large amount of quartz, and consequently have a relatively low *Vp*/*Vs* ratio. Christensen (1996) also found that *Vp*/*Vs* seems to be insensitive to temperature when temperature is far below the solidus. However, when temperature is close enough to the solidus to generate partial melt, the *Vp*/*Vs* ratio is highly sensitive to the amount of melt. Watanabe (1993) found that *Vp*/*Vs* increases significantly with increasing melt fraction, and can reach 2 when melt fraction is above 10 vol%.

Therefore, the large difference in *Vp*/*Vs* ratio between the SE Tibet and its surrounding areas can be caused by a difference in composition or melts, i.e., the crust beneath the SE Tibetan plateau either is more mafic on average or contains more melts compared with the other regions, especially the Yungui plateau. Although our data have no resolution on this ambiguity, there are at least two lines of evidence that suggest melt content is less likely the cause here. First, the SE Tibet, Yungui plateau and NE Tibet have roughly the same heat flux, suggesting that the

thermal structure of the three regions is comparable. Second, the measured seismic velocity beneath the SE Tibet (e.g., Wang et al., 2003; Yao et al., 2010) is not at a low enough level to indicate significant partial melting. We thus conclude that the average composition of the SE Tibetan crust is more mafic, as compared to the crust beneath the Yungui plateau. In other words, a crustal column taken from the SE Tibetan plateau contains a larger portion of mafic lower crustal materials.

4.3. Crustal anisotropy

As mentioned in the discussion, measuring shear wave splitting with receiver function data is really challenging due to the low SNR of the Moho Ps conversion phase. We have applied both harmonic and statistical analyses to ensure that the estimated splitting parameters are not artifacts. As a result, we are able to obtain only 12 measurements from the 79 stations, which are shown in Fig. 7 and listed in the Table 1S (bold italic). We should point out here that for a weak anisotropic or an isotropic medium, the Ps arrival is not expected to show a degree-2 azimuthal variation, and the difference between receiver functions before and after the correction of seismic anisotropy, which lies at the center of the SNR test of Liu and Niu (2012), is expected to be insignificant. These stations were not included in our count. There are 13 stations (Table 1S) with a measured splitting time less than 0.2 s, suggesting that the crust beneath these stations is weakly anisotropic or isotropic. These 13 stations are located inside the Sichuan basin (2), the Yungui plateau (5), the western Yunnan fold systems and belts (4), and the South China fold system (2).

The measured delay times from the 12 stations vary between 0.24 s and 0.9 s, with an average of 0.53. The delay times appear to increase with the Ps arrival time relative to the direct P wave (Fig. 8). The differential travel time between the Ps conversion phase and the direct P, δt_{Ps-P}, roughly equals to the subtraction of the P-wave travel time from the S-wave travel time in the crust. The S-wave travel time of the Ps conversion phase inside the crust is approximately 2.2 times of δt_{Ps-P}. We have also shown the predicted delay times of two anisotropic models in Fig. 8. The dotted lines is the predict splitting time of the Ps arrival with a 5% seismic anisotropy uniformly distributed within the whole crust, while the solid line is the prediction based on an anisotropic model with 6% azimuthal anisotropy (~0.0165 s per kilometer) being evenly distributed inside the lower crust 15 km below Earth's surface. Mica and amphibole are two strongly anisotropic crustal minerals. Tatham et al. (2008) found that amphibole tends to align preferentially through deformation and can generate up to 13% seismic anisotropy under strong shear. Thus the observed 6% seismic anisotropy can be caused by lattice preferred orientation (LPO) of amphibole associated with the lower crustal flow. On the other hand, Lloyd et al. (2009) found that composite S–C fabrics are usually developed when micaeous rocks are naturally deformed, and the estimated seismic anisotropy of the S–C fabrics is between 5.8% and 7.5%. They further found that mixtures of multiple foliations could generate significant variations in the geometry of the seismic anisotropy. If this is the case then it is difficult to generate the observed 6% azimuthal anisotropy with mica fabrics.

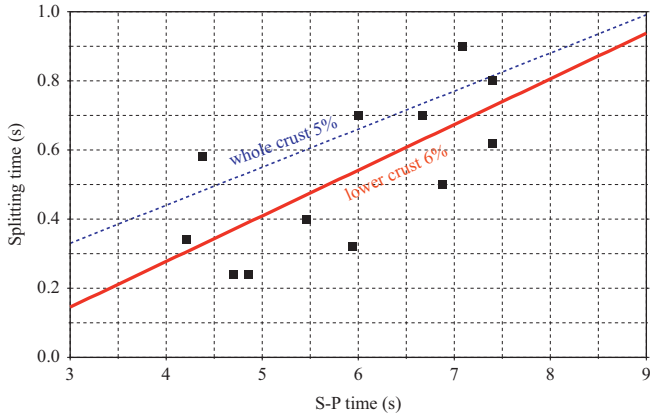

Fig. 8. Splitting times are shown as a function of the S–P travel time. Note the good correlation between the two. Dotted line shows the predicted splitting time from a model with 5% azimuthal anisotropy distributed evenly in the whole crust. The solid line is the prediction from a model with 6% seismic anisotropy only inside the lower crust (defined between 15 km deep and the Moho).

The average splitting time of the 12 measurements is 0.53 s, very close to the 0.58 s averaged delay time measured from the SKS/SKKS data recorded by the MIT/CIGMR array (Lev et al., 2006). The splitting time averaged from the stations located on the Tibetan plateau and its eastern edge is 0.70 s (Fig. 7), which is comparable to the ~1 s global average of SKS/SKKS splitting time, and is also consistent with the surface wave data by Yao et al. (2010), who observed a ~1 s azimuthal anisotropy inside the crust of the SE Tibetan plateau. A station-by-station comparison of the fast polarization direction and splitting time between our measurements and the SKS/SKKS results (Lev et al., 2006) can be found in Table 1S. We find that the 6 stations located on the Tibetan plateau have a fast polarization similar or very close to, and a delay time comparable to the SKS/SKKS measurements. The agreement between the SKS/SKKS and receiver function data suggests that crustal anisotropy is likely the major source of the observed shear wave splitting of the core phases SKS and SKKS. Lev et al. (2006) found a prominent transition in the SKS/SKKS fast polarization direction at the latitude of ~26°N. We have 4 stations located in the southern region that showed an average azimuthal anisotropy of ~0.39 s. The largest splitting time (0.58 s) is observed at station YN.YUJ, which is located near the Red River fault (Fig. 7). The fault is known to have an annual slip rate of ~7 mm per year (Shen et al., 2005), and the observed large splitting is likely the result of the accumulated simple shear along the fault. Neither the measured fast polarization direction nor the observed splitting times match with the SKS/SKKS results, which showed a dominant EW fast polarization direction with delay times between 0.28 and 0.75 s (Lev et al., 2006).

The good agreement of the shear wave splitting measured from the two radially polarized S-wave conversions at the core–mantle boundary (SKS) and the Moho (Pds) at stations on the SE Tibetan plateau provides a strong constraint on the deformation style in the crust and mantle, as well as on possible mechanisms for how the plateau has been uplifted. First, the combination of our results with the SKS data suggest that the upper mantle beneath the SE Tibetan plateau has little to no azimuthal anisotropy. This is inconsistent with the surface wave study of Yao et al. (2010), which found that the mantle lithosphere has some azimuthal anisotropy with a fast polarization direction different from that of the crust. In principle, a depth varying anisotropy is measurable with SKS splitting data, if there is enough sampling from events that occurred over a wide range of back azimuths. This azimuthal coverage could be difficult to achieve with a one or two-year temporary deployment, such as the MIT/CIGMR array (Lev et al., 2006), but it eventually will become possible with the CEA permanent station data. We will leave it to future studies to resolve this issue. We share the same interpretation with Yao et al. (2010) in the sense that the crust and mantle beneath the plateau are likely to be decoupled, and have a different deformation style.

In summary, we found two distinct features on the crust beneath the SE Tibetan plateau: (1) a thick crust with a relatively high *Vp*/*Vs* ratio; (2) the crust is strongly anisotropic, with a fast

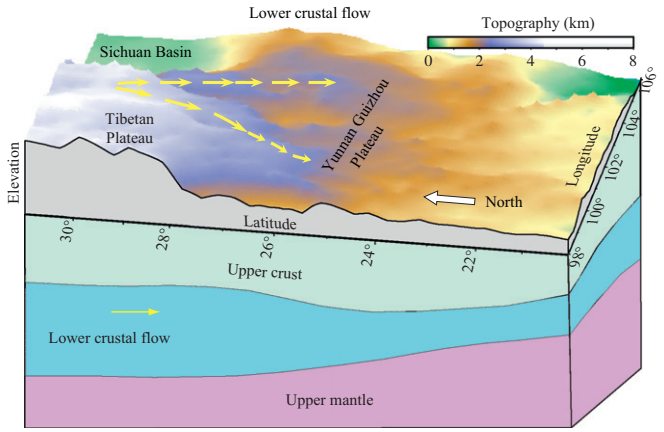

Fig. 9. Cartoon shows the lower crustal flow model and its prediction on the crustal structure and deformation style. Topographic profiles along the west and south sides of the study area are shown in black lines. Arrows on the topographic surface illustrate the direction of the lower crust flow.

direction roughly parallel to the direction of the maximum horizontal tensile stress. These seismic observations provide strong constraints on the nature of deformation beneath SE Tibet. In fact, both observations point to a scenario that lower crustal flow is present beneath SE Tibetan plateau (Fig. 9).

We have argued that the SE Tibetan crust is more mafic in composition than the crust beneath the Yungui plateau based on the observed *Vp*/*Vs* ratio. Now the question is whether the composition difference is inherited during the initial stage of crustal formation or is developed in the late stage of crustal thickening. Although it is almost impossible to use seismic data to argue which one is true, we have some indirect evidence that suggests the difference might have been developed during crustal thickening. First, as mentioned above, to the north of the study area, the NE margin of the Tibetan plateau also has a low *Vp*/*Vs* ratio of ~1.69, which may suggest that the initial crust in the study area is rather felsic. If this is the case, then the thickened crust is unlikely caused by whole crustal shortening, as the process preserves the felsic composition of the original crust, and consequently cannot explain the high *Vp*/*Vs* ratio. On the other hand, the lower crustal flow model can readily explain the elevated *Vp*/*Vs* ratio of the SE Tibetan crust. According to Clark and Royden (2000), lower crust materials flow from the center of the Tibetan plateau to its edge due to an elevation-induced pressure contrast between the plateau and its surroundings. Hacker et al. (2000) studied the deep crustal xenoliths from the central Tibetan plateau and found that the xenoliths erupted from a depth of 30–50 km and were comprised of mafic rocks and siliciclastic metasedimentary rocks. The calculated Poisson's ratio of the xenoliths is ~0.27, equivalent to a *Vp*/*Vs* ratio of ~1.78. Adding these mafic rocks to the original felsic crust can boost the *Vp*/*Vs* ratio to the observed level of ~1.79.

The S-wave ray path of the Moho Ps conversion goes from the Moho to the surface, and the anisotropy can in principle be anywhere along the path. As the fast direction is almost perpendicular to the direction of the maximum horizontal compressional stress, we argue that it is unlikely caused by stress-induced alignment of cracks in the upper crust above ~15 km, and more likely results from fabric structure developed in the lower crust below ~15 km. To produce the amount of seismic anisotropy, a moderate to strong shear is required. Again, the existence of such shear zones is consistent with the lower crustal flower model.

Our results, combined with the SKS data, can also offer some insights into mantle processes beneath the plateau. The simplest interpretation is that the mantle has little deformation. The other possibility is that vertical flow is the primary mode of mantle deformation, and partial lithosphere removal may have been occurring beneath this part of the Tibetan plateau. This is consistent with recent study of Niu (2011), which measured the depth of the lithosphere and asthenosphere boundary (LAB) beneath China with ScS reverberation data and found that the lithosphere beneath the study area is very thin (~80–100 km). Since the crust is 50–70 km thick beneath the SE Tibet plateau, the mantle lithosphere here is only 10–50 km thick. If the original mantle lithosphere is ~100–150 km thick, then a large portion of the mantle lithosphere must have been removed. Studies of rock mechanics indicated that most of the strength of continental lithosphere is contained in two separate strong zones, one in the upper crust and one in the upper mantle (e.g., Brace and Kohlstedt, 1980). It has been shown that an increase in crustal thickness or a decrease in lithosphere thickness can reduce the overall strength of the lithosphere (Dunbar and Sawyer, 1988). We speculate that the high level of seismicity observed in the study region reflects the weakness of the lithosphere, which is made up primarily of crust rocks.

5. Conclusion

We investigate crustal structure and seismic anisotropy beneath the SE Tibetan plateau and its surrounding areas with receiver function data. We find that the crust beneath the SE Tibetan plateau has a thickness of ~50–70 km and a relatively high *Vp*/*Vs* ratio of ~1.79. The latter suggests that mafic lower crustal materials compose a significant portion of the crust beneath the SE margin of the Tibetan plateau. We also find that the crust beneath the SE Tibetan plateau is highly anisotropic, with fast polarization directions and splitting times comparable to those measured from SKS/SKKS data, suggesting that deformation in the upper mantle is either very weak or primarily in the vertical direction, different from that seen in the crust. These observations are consistent with a scenario of lower crustal extrusion beneath the margin.

Acknowledgments

We thank the Data Management Center of the China Earthquake Administration for providing the waveform data for this study. We also thank Min Chen, Yuan Gao, Steve Grand, and Alan Levander for discussion, and two anonymous reviewers for their critical review and constructive comments, which significantly improved the quality of this paper. This study is supported by the NSF grant EAR-063566 and the Fundamental Research Funds for the Central Universities of Central South University.

Appendix A. supplementary material

Supplementary data associated with this article can be found in the online version at http://dx.doi.org/10.1016/j.epsl.2012.07.007.

References

Ammon, C.J., 1991. The isolation of receiver effect from teleseismic p waveforms. Bull. Seismol. Soc. Am. 81, 2504–2510.

Bai, D., Unsworth, M.J., Meju, M.A., Ma, X., Teng, J., Kong, X., Sun, Y., Sun, J., Wang, L., Jiang, C., Zhao, C., Xiao, P., Liu, M., 2010. Crustal deformation of the eastern Tibetan plateau revealed by magnetotelluric imaging. Nat. Geosci. 3, 358–362, http://dx.doi.org/10.1038/ngeo830.

Brace, W.F., Kohlstedt, D.L., 1980. Limits on lithospheric stress imposed by laboratory experiments. J. Geophys. Res. 85(B11): http://dx.doi.org/10.1029/0JGREA000085000B11006248000001. issn: 0148-0227.

Chen, Y.L., Niu, F., Liu, R.F., Huang, Z.B., Tkalcic, H., 2010. Crustal structure beneath China from receiver function analysis. J. Geophys. Res. 115, B03307, http://dx.doi.org/10.1029/2009JB006386.
Christensen, N.I., 1996. Poisson's ratio and crustal seismology. J. Geophys. Res. 101, 3139–3156.
Clark, M.K., Royden, L.H., 2000. Topographic ooze: building the eastern margin of Tibet by lower crustal flow. Geology 28, 703–706.
Clark, M.K., House, M.A., Royden, L.H., Whipple, K.X., Burchfiel, B.C., Zhang, X., Tang, W., 2005. Late Cenozoic uplift of southeastern Tibet. Geology 33, 525–528, http://dx.doi.org/10.1130/G21265.1.
Crampin, S., Lovell, J.H., 1991. A decade of shear-wave splitting in the Earth's crust: what does it mean? what use can we make of it? and what should we do next?. Geophys. J. Int. 107, 387–407.
Dunbar, J.A., Sawyer, D., 1988. Continental rifting at pre-existing lithospheric weaknesses. Nature 333, 450–452.
Hacker, B.R., Gnos, E., Ratschbacher, L., Grove, M., McWilliams, M., Sobolev, S., Wan, J., Wu, Z.H., 2000. Hot and dry deep crustal xenoliths from Tibet. Science 287, 2463–2466.
Kawakatsu, H., Niu, F., 1994. Seismic evidence for a 920-km discontinuity in the mantle. Nature 371, 301–305.
Kennett, B.L., Engdahl, E.R., 1991. Travel times for global earthquake location and phase identification. Geophys. J. Int. 105, 429–465.
Lev, E., Long, M.D., van der Hilst, R.D., 2006. Seismic anisotropy in Eastern Tibet from shear wave splitting reveals changes in lithospheric deformation. Earth Planet. Sci. Lett. 251, 293–304.
Levin, V., Park, J., 1997. P-SH conversions in a flat-layered medium with anisotropy of arbitrary orientation. Geophys. J. Int. 131, 253–266.
Liu, H., Niu, F., 2012. Estimating crustal seismic anisotropy with a joint analysis of radial and transverse receiver function data. Geophys. J. Int. 188, 144–164, http://dx.doi.org/10.1111/j.1365-246X.2011.05249.x.
Lloyd, G., Butler, R., Casey, M., Mainprice, D., 2009. Mica, deformation fabrics and the seismic properties of the continental crust. Earth Planet. Sci. Lett. 288, 320–328, http://dx.doi.org/10.1016/j.epsl.2009.09.035.
Mainprice, D., Nicolas, A., 1989. Development of shape and lattice preferred orientations: application to the seismic anisotropy of the lower crust. J. Struct. Geol. 11, 175–189.
McNamara, D.E., Owens, T.J., 1993. Azimuthal shear wave velocity anisotropy in the Basin and Range Province using Moho Ps converted phases. J. Geophys. Res. 98, 12003–12017.
Muirhead, K.J., 1968. Eliminating false alarms when detecting seismic events automatically. Nature 217, 533–534.
Nair, S.K., Gao, S.S., Liu, K.H., Silver, P.G., 2006. Southern African crustal evolution and composition: constraints from receiver function studies. J. Geophys. Res. 111, B02304, http://dx.doi.org/10.1029/2005JB003802.
Nicolas, A., Christensen, N.I., 1987. Formation of anisotropy in upper mantle peridotites—a review. In: Fuchs, K., Froideveaux, C. (Eds.), Composition, Structure and Dynamics of the Lithosphere–Asthenosphere System, Geodynamics Series, vol. 16. American Geophysical Union, Washington, D.C., pp. 111–123.
Niu, F., Kawakatsu, H., 1998. Determination of the absolute depths of the mantle transition zone discontinuities beneath China: effect of stagnant slabs on mantle transition zone discontinuities. Earth Planet. Sci. Lett. 50, 965–975.
Niu, F., James, D.E., 2002. Fine structure of the lowermost crust beneath the Kaapvaal craton and its implications for crustal formation and evolution. Earth Planet. Sci. Lett. 200, 121–130, http://dx.doi.org/10.1016/S0012-821X0200584-8.
Niu, F., Baldwin, T., Pavlis, G., Vernon, F., Rendon, H., Bezada, M., Levander, A., 2007. Receiver function study of the crustal structure of the Southeastern Caribbean Plate Boundary and Venezuela. J. Geophys. Res. 112, B11308, http://dx.doi.org/10.1029/2006JB004802.
Niu, F., Li, J., 2011. Component azimuths of the CEArray stations estimated from P wave particle motion. Earthquake Sci. 24, 3–13, http://dx.doi.org/10.1007/s11589-011-0764-8.
Niu, F., 2011. Mapping lithosphere thickness beneath China with ScS reverberation data: what controls the intraplate seismicity in Mainland China. Abstract S23E-02 presented at 2011 Fall Meeting, AGU, San Francisco, Calif, 5–9 December 2011.
Pan, S., Niu, F., 2011. Large contrasts in crustal structure and composition between the Ordos plateau and the NE Tibetan plateau from receiver function analysis. Earth Planet. Sci. Lett. 303, 291–298, http://dx.doi.org/10.1016/j.epsl.2011.01.007.
Peng, X., Humphreys, E.D., 1997. Moho dip and crustal anisotropy in northwestern Nevada from teleseismic receiver functions. Bull. Seismol. Soc. Am. 87, 745–754.
Royden, L.H., Burchfiel, B.C., King, R.W., Wang, E., Chen, Z., Shen, F., Liu, Y, 1997. Surface deformation and lower crustal flow in eastern Tibet. Science 276, 788–790.
Savage, M.K., 1998. Lower crustal anisotropy or dipping boundaries? Effects on receiver functions and a case study in New Zealand. J. Geophys. Res. 103, 15069–15087.
Shen, Z.K., Lu., J.J., Wang, M., Burgmann, R., 2005. Contemporary crustal deformation around the southeast borderland of the Tibetan plateau. J. Geophys. Res. 110, B11409, http://dx.doi.org/10.1029/2004JB003421.
Shiomi, K., Park, J., 2008. Structural features of the subducting slab beneath the Kii Peninsula, central Japan: seismic evidence of slab segmentation, dehydration, and anisotropy. J. Geophys. Res. 113, B10318, http://dx.doi.org/10.1029/2007JB005535.
Silver, P.G., 1996. Seismic anisotropy beneath the continents: probing the depths of Geology. Annu. Rev. Earth Planet. Sci. 24, 385–432.
Schoenbohm, L.M., Burchfiel, B.C., Chen, L., 2006. Propagation of surface uplift, lower crustal flow, and Cenozoic tectonics of the southeast margin of the Tibetan plateau 34, 813–816, http://dx.doi.org/10.1130/G22679.1.
Sun, Y., Toksoz, M.N., 2006. Crustal structure of China and surrounding regions from P wave traveltime tomography. J. Geophys. Res. 111, B03310, http://dx.doi.org/10.1029/2005JB003962.
Tatham, D.J., Lloyd, G.E., Butler, R.W.H., Casey, M., 2008. Amphibole and lower crustal seismic properties. Earth Planet. Sci. Lett. 267, 118–128.
Tarkov, A.P., Vavakin, V.V., 1982. Poisson's ratio behavior in crystalline rocks: application to the study of the Earth's interior. Phys. Earth Planet. Inter. 29, 24–29, http://dx.doi.org/10.1016/0031-9201(82)90134-0.
Tapponnier, P., Peltzer, G., Le Dain, A.Y., Armijo, R., Cobbold, P., 1982. Propagating extrusion tectonics in Asia: new insights from simple experiments with plasticine. Geology 10, 611–616.
Tapponnier, P., Lacassin, R., Leloup, P.H., Schärer, U., Zhong, D., Wu, H., Liu, X., Ji, S., Zhang, L., Zhong, J., 1990. The Ailao Shan/Red River metamorphic belt: tertiary left-lateral shear between Indochina and South China. Nature 343, 431–437.
Vinnik, L.P., 1977. Detection of waves converted from P to SV in the mantle. Phys. Earth Planet. Inter. 15, 39–45.
Wang, C.Y., Chan, W.W., Mooney, W.D., 2003. Three-dimensional velocity structure of crust and upper mantle in southwestern China and its tectonic implications 108 (B9), 2442, http://dx.doi.org/10.1029/2002JB001973.
Watanabe, T., 1993. Effects of water and melt on seismic velocities and their application to characterization of seismic reflectors. Geophys. Res. Lett. 20 (2), 933–2936.
Wang, C.Y., Flesch, L.M., Silver, P.G., Chang, L.J., Chan, W.W., 2008. Evidence for mechanically coupled lithosphere in central Asia and resulting implication. Geology 36, 363–366, http://dx.doi.org/10.1130/G24450A.1.
Watson, M., Hayward, A.B., Parkinson, D.N., Zhang, Z.M., 1987. Plate tectonic history, basin development and petroleum source rock deposition onshore China. Mar. Pet. Geol. 4, 205–225.
Xu, L., Rondenay, S., van der Hilst, R.D., 2007. Structure of the crust beneath the southeastern Tibetan plateau from teleseismic receiver functions. Phys. Earth Planet. Inter. 165, 176–193.
Yao, H., Beghein, C., van der Hist, R.D., 2008. Surface wave array tomography in SE Tibet from ambient seismic noise and two-station analysis: II. Crustal and upper-mantle structure. Geophys. J. Int. 163, 205–219, http://dx.doi.org/10.1111/j.1365-246X.2007.03696.x.
Yao, H., Van der Hilst, R.D., Montagner, J.P., 2010. Heterogeneity and anisotropy of the lithosphere of SE Tibet from surface wave array tomography. J. Geophys. Res. 115, B12307, http://dx.doi.org/10.1029/2009JB007142.
Yin, A., Harrison, T.M., 2000. Geologic evolution of the Himalayan-Tibetan orogen. Annu. Rev. Earth Planet. Sci. 28, 211–280.
Zhu, L., Kanamori, H., 2000. Moho depth variation in southern California from teleseismic receiver functions. J. Geophys. Res. 105, 2969–2980.